Scientia Iranica (2024) 31(14), 1206–1221

SCIENTIA
IRANICA

Sharif University of Technology
Scientia Iranica
Transactions D: Computer Science & Engineering and Electrical Engineering
https://scientiairanica.sharif.edu

Control and performance assessment of grid-connected PMSG-based wind turbine equipped with diode bridge rectifier and boost converter using three different control strategies

Y. Abdollahi, M. Rahimi*, and A. Halvaei Niasar

Department of Electrical and Computer Engineering, University of Kashan, Kashan, P.O. Box 87317-53153, Iran.

Received 5 September 2021; received in revised form 20 March 2022; accepted 11 July 2022

KEYWORDS
PMSG-based wind turbine;
Boost converter;
Machine-side converter;
Sensorless control strategies;
Transient and LVRT behavior.

Abstract. In this paper, as the main contribution, three sensorless control structures are presented for the control of the grid-connected PMSG-based Wind Turbine (WT) employing boost converter and diode rectifier as the machine-side converter. Then, detailed control structures of the boost converter and grid-side converter at the three mentioned control strategies are extracted, and next, features of the abovementioned control strategies are investigated and compared against wind speed variation and grid voltage dip. The boost converter, in the first control strategy, controls the generator speed at the Maximum Power Point Tracking (MPPT) mode, and in the second control strategy, it regulates the Permanent Magnet Synchronous Generator (PMSG) active power to its set point value. Also, the boost converter, in the third control strategy, adjusts the voltage of the dc-link capacitor to its set point value. In this paper, steady-state performance and transient/LVRT behavior of the WT system are examined for each mentioned control strategy in the MATLAB-Simulink environment. It is shown that WT steady-state responses are relatively identical for all three control strategies. However, as an interesting result, at the fault conditions, the third control strategy has superior performance, and thus, the WT fault ride-through behavior enhances significantly with the third control structure without any hardware protection.

1. Introduction

Currently, full converter-based Wind Turbines (WTs) with Permanent Magnet Synchronous Generators (PMSGs), known as PMSG-based WTs, are widely used in WT industry and grid-connected applications. PMSG-based WTs have substantial advantages such as simple structure, enhanced power factor, lower maintenance cost and wider speed range in maximum power operation mode [1–5].

---

*. *Corresponding author.*
E-mail address: mrahimi@kashanu.ac.ir (M. Rahimi)

To cite this article:
Y. Abdollahi, M. Rahimi, and A. Halvaei-Niasar "Control and performance assessment of grid-connected PMSG-based wind turbine equipped with diode bridge rectifier and boost converter using three different control strategies", *Scientia Iranica* (2024) **31**(14), pp. 1206-1221
https://doi.org/ 10.24200/sci.2022.58983.6001

PMSG-based WTs are attached to the grid via cascaded power electronics converters, called Machine and Grid Side Converters (MSC and GSC). Considering the MSC structure, in PMSG-based WTs, the MSC can be a Voltage Source Converter (VSC) [6,7] or combination of the boost converter and diode-rectifier can be used as the MSC [8–10]. Numerous papers have discussed about the control and performance analysis of the PMSG-WTs with back-to-back frequency converters. A number of papers have also dealt with the behavior analysis and control of PMSG-WTS employing combination of boost converter and diode-rectifier as the MSC [8–24].

In [8], PMSG-WT stability and impact of speed controller parameters on the WT stability is studied by the modal analysis. Ref. [9] focuses on studying the oscillation modes of direct driven PMSGs connected to the power grid by developing small signal models of PMSG-based WTGS with different converter topologies. In [10], it is dealt with the modification of the boost converter control for improving the PMSG-WT performance. Refs. [11–13] discusses regarding the sensorless performance of small PMSG-WTs with diode bridge rectifier in the maximum power mode. In [14], a maximum power mode approach, known as incremental conductance approach, is presented for small PMSG-WT supplying a dc-load. In [15], sliding mode control with improving transient approach is suggested for the PMSG-based WT control, in which diode rectifier, boost converter, Neutral Point Clamped (NPC) inverter and L-filter are used as the interface between the WT and grid. In [16], second-order sliding mode control are designed as voltage regulators for generating the control signal to bring the system to optimal boost converter voltage for realizing Maximum Power Point Tracking (MPPT). In [17], power control of 5-phase PMSG-diode rectifier set associated to 3-interleaved boost converter is investigated, and in [18–21], model predictive control are used for the PMSG-based WT control assisted with boost converter and diode rectifier. In [22–24], PMSG-WT supported by the boost converter is used for supplying stand-alone load. Ref. [25] proposes three topologies of single-stage three-phase ac-dc buck-boost converters suitable for medium-voltage and high-power wind energy conversion systems that reduce the voltage and current stresses on the self-commutated switching device compared to existing solutions.

Usually, grid-connected PMSG-WTs are controlled based on two control structures, where in the first control structure [7–10,26–29], the MSC adjusts the generator speed and the GSC sets the dc-link voltage, and, in the second control structure [6,30–35], the MSC controls the voltage of the dc-link capacitor and the GSC regulates the injected power to the grid.

The subject of this paper is about the control and performance analysis of the PMSG-WT implementing boost converter as the MSC, as depicted in Figure 1. This research is a continuation of the previous papers [8,10], where in both [8] and [10], the PMSG-WT uses boost converter and diode-rectifier and WT is controlled based on the first control structure, in which the boost converter adjusts the generator speed to a value corresponding to MPPT mode. In [8], small-signal stability analysis of the PMSG-WT is presented and impact of the speed controller parameters on the WT stability is investigated by the modal analysis. Also, in [10] modification of the control system of the boost converter for improving the PMSG-WT performance is presented.

In this paper, as the main contribution, three sensorless control structures are presented for the control of the PMSG-WT employing boost converter and diode-rectifier as the machine converter, and then responses of the mentioned control strategies are compared. In this way, first, the relationship between the active component of the stator current and boost converter current is extracted, and then a simple and efficient approach is presented for the generator speed estimation. Next, detailed control structures of the converters at the three mentioned control strategies are extracted and given. In the first control strategy, the boost converter is responsible for the control of the generator speed at the MPPT mode and GSC is used for regulation of the dc-link voltage. In the second control strategy, the boost converter is used to set the PMSG active power at the reference value, and GSC adjusts the dc-link voltage to its reference value. In the third control strategy, the boost converter regulates the dc-link voltage at the reference value, and GSC controls

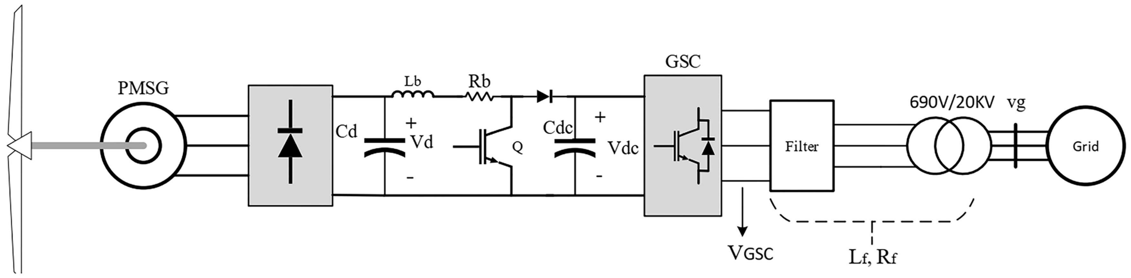

Figure 1. Overall structure of the system under study.

the injected active power to the grid to a reference value corresponding to the MPPT mode. In the paper, steady-state performance and transient/LVRT behavior of the WT system are examined for each mentioned control strategy. It is shown that WT steady-state responses are relatively identical for all three control strategies. However, at the fault conditions, the third control strategy has better performance, and thus, the WT low voltage ride-through behavior improves significantly by using the third control structure without any hardware protection.

The paper is organized as follows. In Sections 2 and 3, mathematical modeling, current control and steady-state behavior of the study system are presented. In Section 4, three strategies are presented for the PMSG-WT control, and then, control loops of the boost converter and grid-side converter are extracted in each control strategy. Finally, in Section 5, time domain simulation results are given, and steady-state and transient capabilities of the three presented control strategies are compared and investigated. Finally, conclusion is explored in Section 6.

2. Mathematical representation of the PMSG with diode rectifier

This section presents dynamic modeling of the PMSG and current control of the boost converter and GSC. In this study, for the PMSG modeling, the stator currents direction is considered into the stator windings.

The stator voltages and fluxes of a cylindrical pole PMSG, in the rotor dq reference frame with rotational speed of ω_r, can be given as [9]:

$$v_{dq} = R_s i_{dq} + j\omega_r \psi_{dq} + \frac{d\psi_{dq}}{dt}, \tag{1}$$

$$\begin{cases} \psi_d = L_s i_d + \psi_{pm} \\ \psi_q = L_s i_q \end{cases} \tag{2}$$

where v, i, and ψ stand for the stator voltage, current, and flux, ψ_{pm} is the stator flux linkage due to rotor permanent magnet, R_s is the stator resistance, and L_s is the stator synchronous inductance. Also, ω_r is the rotor rational speed, that at steady-state conditions is identical to the stator frequency, ω_s. Besides, the generator electromechanical torque in a cylindrical pole PMSG is given by:

$$T_e = \frac{3}{2}\frac{p}{2}\left(\psi_{pm} i_{sq}\right), \tag{3}$$

where p denotes the number of generator poles.

2.1. Current control of boost converter

In Figure 1, the boost converter is interfaced between the diode rectifier and grid-side converter, and by varying the duty cycle of the switch Q, the inductor current i_b can be controlled. Considering the Continuous Conduction Mode (CCM) operation of the boost converter, two different cases related to *on* and *off* states of the switch Q can be considered. The boost converter average model over one switching cycle is achieved, as given in Figure 2.

From Figure 2, the dynamics of the boost converter current is achieved as:

$$v_d = R_b i_b + L_b \frac{di_b}{dt} + v_{dc}(1-d), \tag{4}$$

where d denotes the switch Q duty cycle. Considering $d = d_0 + \Delta d$, $v_d = v_{d0} + \Delta v_d$, $i_b = i_{b0} + \Delta i_b$, and $v_{dc} = v_{dc0} + \Delta v_{dc}$, the small-signal model of the boost converter current dynamics is obtained as given in Eq. (5), where the symbols Δ and 0 represent the small-signal variation, and operating point, respectively:

$$L_b \frac{d\Delta i_b}{dt} + R_b \Delta i_b = \Delta d . v_{dc0} - \Delta v_{dc}(1-d_0) + \Delta v_d. \tag{5}$$

From Eq. (5) and by considering the boost converter controller as the PI type, the current control loop of the boost converter is obtained as given in Figure 3, where the control signal d regulates i_b to its set point value.

By implementing the pole-zero deletion approach in Figure 3, we have $k_p/k_i = R_b/L_b$, and by choosing $k_p = \alpha_b L_b$, the transfer function from i_{b-ref} to i_b is achieved as:

$$\frac{i_b(s)}{i_b(s)^*} = \frac{\alpha_b}{s + \alpha_b}, \tag{6}$$

where α_b denotes the current control closed loop bandwidth, which is selected sufficiently smaller than the converter switching frequency ω_{sw}.

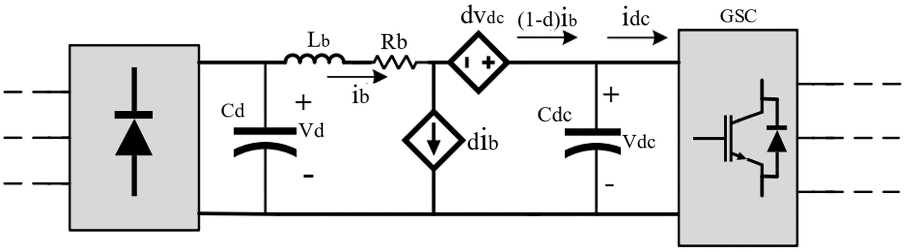

Figure 2. Average model of the boost converter over one switching cycle.

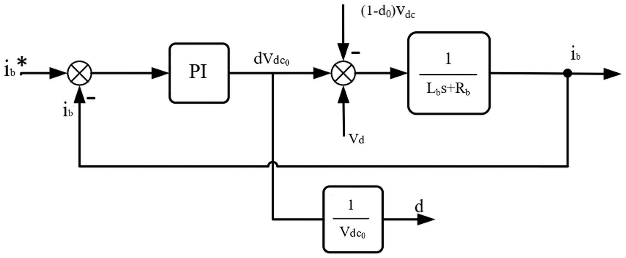

Figure 3. Boost converter current control loop.

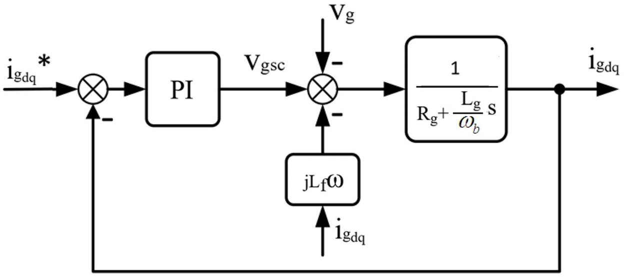

Figure 4. Current control loops of the GSC in the *dq* reference frame.

2.2. Current control of the GSC

The GSC, in Figure 1, is linked to the grid through interfaced passive filter and step-up transformer, where the filter and transformer are specified by inductance L_f and resistance R_f. The dynamics of the GSC current, in pu, is given by:

$$v_{GSCdq} = R_f i_{gdq} + j\omega L_f i_{gdq} + \frac{L_f}{\omega_b}\frac{di_{gdq}}{dt} + v_{gdq}, \quad (7)$$

where v_{GSCdq}, i_{gdq}, and v_{gdq} are the *dq*-components of the GSC output voltage and current and grid voltage, respectively. Figure 4 shows the control loops of the GSC *dq* axes currents.

The GSC is normally controlled in the *dq* frame with the Grid Voltage Orientation (GVO), in which $v_{gd} = |v_g|$, and $v_{gq} = 0$. In GVO, i_{gd} is the active power part of the GSC current used for regulation of the output active power or dc-link voltage.

Considering the WT control strategy, the GSC may regulate the dc-link voltage or the active power injected to the grid, and thus i^*_{gd} is achieved from the outer dc-link voltage control loop or outer active power control loop, as will be given in Section 4. Also, in the GVO reference frame, i_{gq} is the reactive power component of the GSC current used for the reactive power/grid voltage control.

3. Steady state behavior of the PMSG-WT with boost converter and diode rectifier

By equating the stator flux derivative to zero and from Eqs. (1) and (2), the steady-state model of the surface mounted PMSG is achieved as given in Eq. (8):

$$v_{sdq} = R_s i_{sdq} + jX_s i_{sdq} + j\omega_r \psi_{pm}. \quad (8)$$

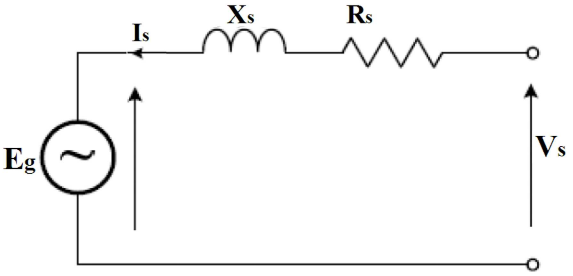

Figure 5. One-phase equivalent circuit of the PMSG.

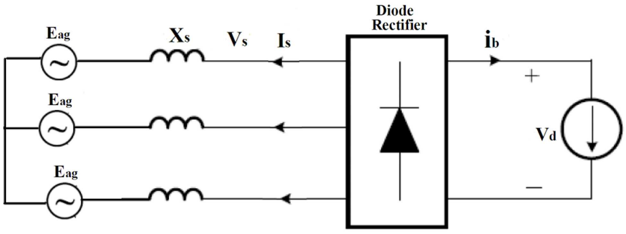

Figure 6. PMSG and boost converter equivalent circuit at steady state conditions.

Considering (8), Figure 5, depicts the one-phase circuit of the PMSG at steady-state conditions, where $E_g = j\omega_r\psi_{pm}$ is the back-emf voltage of the stator, and X_s is the PMSG synchronous reactance.

In the study system of Figure 1, the inductor L_b is selected such that the boost converter works at the Continuous Conduction Mode (CCM). Hence, as depicted in Figure 6, the boost converter at steady state conditions is modeled as a current source at the output of the diode-rectifier.

In Figure 6, E_{abcg} and V_d are the three-phase back-emf voltages, and rectifier output voltage. By ignoring the stator resistance and according to [36], the rectifier average output voltage may be given as:

$$v_d = \frac{3\sqrt{3}}{\pi}|E_g| - \frac{3}{\pi}X_s i_b, \quad (9)$$

where the second term in Eq. (9), i.e., $(3/\pi)X_s i_b$, is the voltage drop at the rectifier output due to synchronous reactance the current commutation in the diode, X_s due to reactance it is noted that. X_s rectifier is not instantaneous causing rectifier output voltage drop.

From Eq. (8) and Figure 5 and by ignoring the stator resistance, the PMSG output active power can be given by:

$$P_s = -\frac{3}{2}|E_g|\, i_{sq} = -\frac{3}{2}\omega_r\psi_{pm} i_{sq}. \quad (10)$$

Because of presence of diode-rectifier, three-phase stator currents comprise higher harmonics, where in the synchronous reference frame, the stator currents with the fundamental frequency become dc terms and other harmonics appear as ripples with frequency of $6\omega_0$ (ω_0 is the fundamental frequency). Hence, the fundamental part of the stator current and accordingly the average component of the q-axis stator current $\bar{i}_{sq}$ are responsible for delivering the PMSG active power. Therefore, the average output active power of the PMSG can be given by:

$$\bar{P}_s = -\frac{3}{2}\left|E_g\right|\bar{i}_{sq} = -\frac{3}{2}\omega_r\psi_{pm}\bar{i}_{sq}, \tag{11}$$

where the superscript $-$ in Eq. (11) denotes the average value. In Figure 6, by neglecting the rectifier losses and equating the average output powers of the PMSG and rectifier, we have:

$$-\frac{3}{2}\left|E_g\right|\bar{i}_{sq} = \left(\frac{3\sqrt{3}}{\pi}\left|E_g\right| - \frac{3}{\pi}X_s i_b\right) i_b. \tag{12}$$

Simulation studies show that at different wind speeds, the term $(3/\pi)\,X_s i_b$ at the right side of Eq. (12) is a fraction of $\left(3\sqrt{3}/\pi\right)\left|E_g\right|$, so that at low wind speeds (about 6 m/s) this ratio is about 0.01 and at nominal wind speeds, this ratio is about 0.1. Given this fact, Eq. (8) can be rewritten as:

$$-\frac{3}{2}\left|E_g\right|\bar{i}_{sq} = (0.9 \sim 0.99)\,\frac{3\sqrt{3}}{\pi}\left|E_g\right| i_b. \tag{13}$$

From Eq. (13), the relationship between i_b and $\bar{i}_{sq}$ is as follows:

$$\bar{i}_{sq} = -\,(0.99 \sim 1.09)\,i_b. \tag{14}$$

Figure 7(b) shows the average values of i_{sq} and boost converter current i_b under wind speed profile of Figure 7(a) for the study 2 MW PMSG-based WT with parameters of Appendix A. Considering Eq. (14) and Figure 7, in a wide range of wind speed variations, the average values of i_{sq} and i_b are approximately identical, i.e., $\left|\bar{i}_{sq}\right| \cong i_b$. Therefore, from Eq. (3), the PMSG torque as a function of i_b is approximately given by:

$$T_e = -\frac{3}{2}\frac{p}{2}n_p\left(\psi_{pm} i_b\right). \tag{15}$$

4. Different control strategies of the study system

In this section according to main duties of the boost converter and GSC, three control strategies are briefly introduced for the study system. In the first control strategy, according to Figure 8(a), the boost converter is responsible for the generator speed control at the MPPT mode and GSC is used for the dc-link voltage control. In the second control strategy, according to Figure 8(b), the boost converter is used to adjust the PMSG active power at the reference value, and GSC adjusts the dc-link voltage to its set point value. In the third control strategy, as clear from Figure 8(c), the boost converter regulates the dc-link voltage, and GSC adjusts the active power injected to the grid to a reference value corresponding to MPPT mode. It is noted that at all three mentioned control strategies, the study system is controlled in the MPPT mode, and the reference of the generator speed/active power is achieved according to the power-speed curve.

Detailed representations and block diagrams of these control strategies will be given in Sections 4.2–4.4.

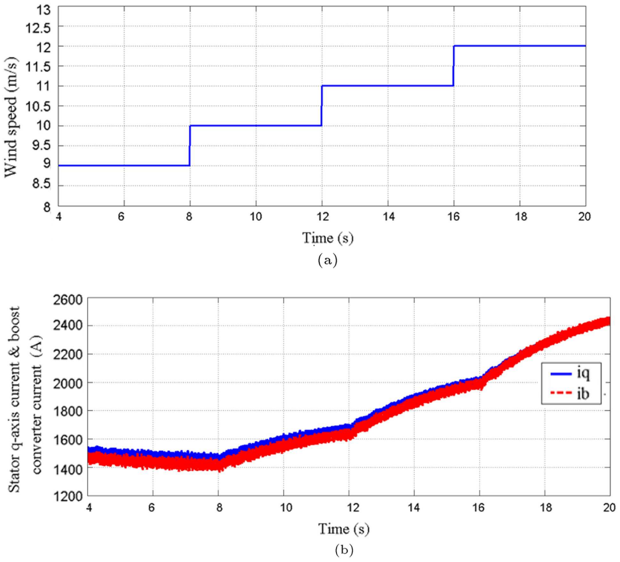

Figure 7. (a) Wind speed profile and (b) comparison of average values of the boost converter current and stator q-axis current under wind speed profile of Figure 7(a).

4.1. *Estimation of rotor speed in PMSG-WT with boost converter and diode rectifier*

In all three mentioned control strategies mentioned above the generator speed is required for the control of the study system. In this section, a method is presented for estimation of the generator speed. According to Eq. (9), the rectifier output voltage v_d may be given as $v_d = v_{d0} - \frac{3}{\pi}X_s i_b$, where the first term $v_{d0} = \left(3\sqrt{3}/\pi\right)\omega_r\psi_{pm} = k\omega_r$, known as no load voltage, is proportional to generator speed, and the second term $\frac{3}{\pi}X_s i_b$ is the voltage drop due to commutation procedure. Table 1 depicts the values of the first and second items at different wind speeds. As stated before, and it is clear from Table 1, the contribution of the term $\frac{3}{\pi}X_s i_b$ in v_d is negligible, and we can approximately

Table 1. Contributions of the first and second items on the average output voltage of the rectifier.

Terms	Wind speed (m/s)			
	6	**8**	**10**	**12**
$\frac{3}{\pi}X_s i_b$	1.27	1.84	4.1	7.51
$\frac{3\sqrt{3}}{\pi}\omega_r\psi_{pm}$	132.82	158.04	208.38	259.58

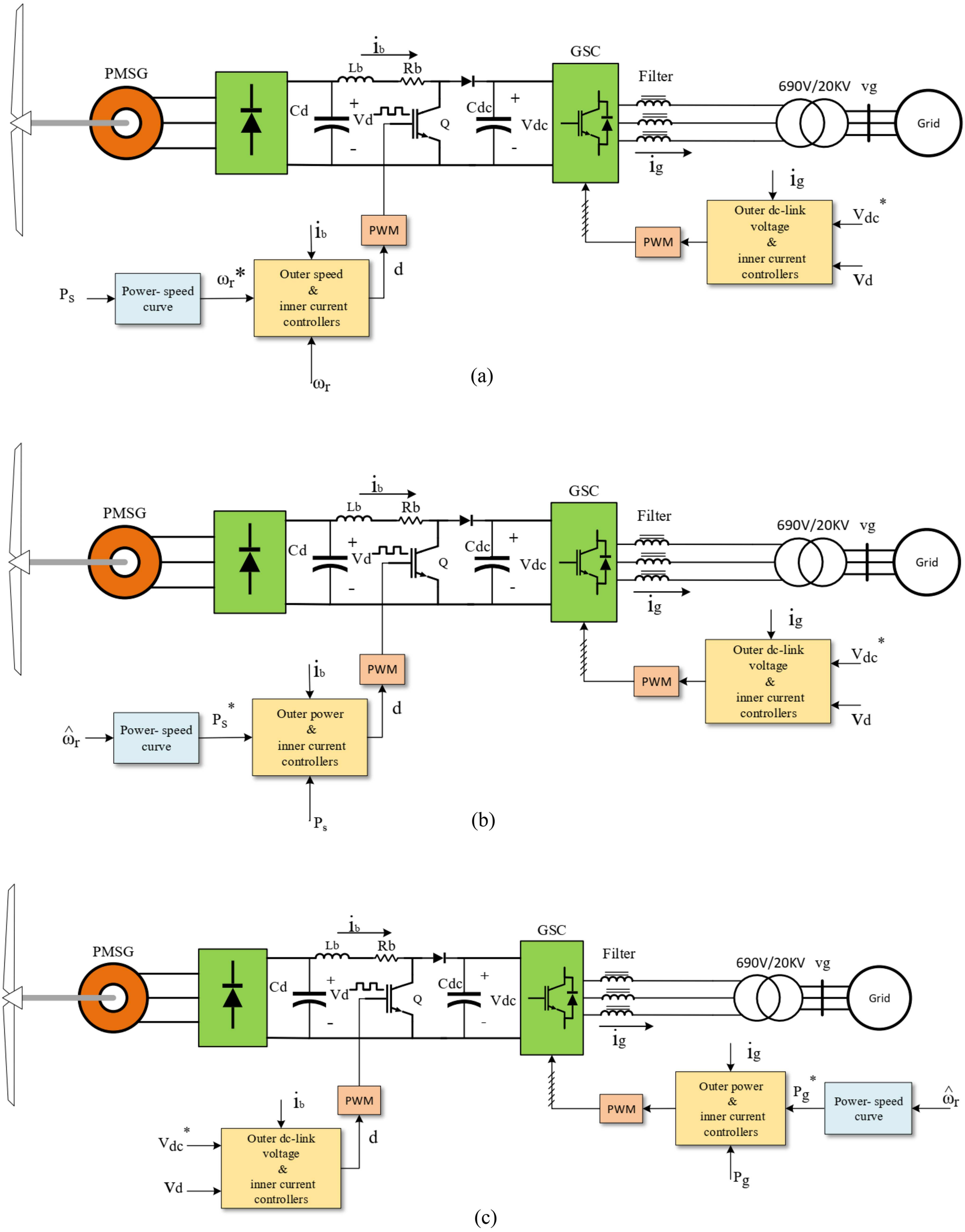

Figure 8. Overall control structures of the study system related to three different control strategies, (a) first control strategy, (b) second control strategy, and (c) third control strategy.

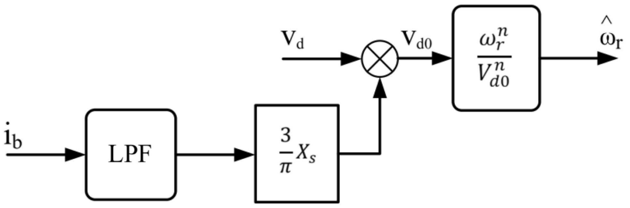

Figure 9. Estimation of the generator speed.

express $v_d \cong \left(3\sqrt{3}/\pi\right)\omega_r\psi_{pm}$. However, since $v_{d0} = k\omega_r$, the accurate estimation of the generator speed can be realized through measuring v_d and computing v_{d0} ($v_d = v_{d0} - \frac{3}{\pi}X_s i_b$). Figure 9 demonstrates the block diagram for accurate estimation of the generator speed, where ω_r^n and v_{d0}^n correspond to rated generator speed and power.

4.2. System control structure at the first control strategy

In this section, the control block diagrams of the boost converter and GSC with the first control strategy are presented.

4.2.1. Boost converter control with the first control strategy

According to Eq. (15), the electromagnetic torque T_e is directly related to the boost converter current i_b. Hence, the generator speed may be controlled by adjusting through duty cycle of boost converter switch. Figure 10 illustrates the overall block-diagram of the boost converter control with the first control strategy. The control structure of the boost converter includes the outer generator speed and inner current control loops, where the boost converter reference current is obtained from the outer control loop of the generator speed.

Figure 11 demonstrates the generator speed control loop, in which $\alpha_b/(s+\alpha_b)$ denotes the transfer function of the boost converter current control loop.

Since the outer speed control loop is much slower than the inner current control loop, in the speed control loop, it is possible to ignore the inner current control dynamics and thus replaces $\alpha_b/(s+\alpha_b)$ with 1. Therefore, the closed-loop transfer function of the generator speed control is achieved as given below:

$$\frac{\omega_r}{\omega_{r-ref}} = \frac{\left(3n_p\psi_{pm}/4H_g\right)\left(k_{p\omega}s + k_{i\omega}\right)}{s^2 + \left(3n_p\psi_{pm}k_{p\omega}/4H_g\right)s + \left(3n_p\psi_{pm}k_{i\omega}/4H_g\right)}. \tag{16}$$

According to Eq. (16), we obtain the parameters of PI controller, $k_{p\omega}$ and $k_{i\omega}$, from the following equation:

$$2\xi\omega_n = \left(3n_p\psi_{pm}k_{p\omega}/4H_g\right),$$
$$\omega_n{}^2 = \left(3n_p\psi_{pm}k_{i\omega}/4H_g\right), \tag{17}$$

where ω_n and ξ correspond to the undamped natural frequency and damping ratio of the control loop, respectively. Due to direct relation between the ω_n and closed loop bandwidth of the outer control loop, ω_n is selected much smaller than the bandwidth of the inner current control loop (α_b), because the dynamics of the outer speed control loop is much slower than the dynamics of the current control loop. Hence, the PI controller parameters of the generator speed control, i.e., $k_{p\omega}$ and $k_{i\omega}$, are obtained from Eq. (17) by setting $\omega_n = 2\pi \times 1$ rad/s and $\xi = 0.7$.

In Figure 11, the reference speed ω_r^* is selected such that the WT works in the MPPT mode at the

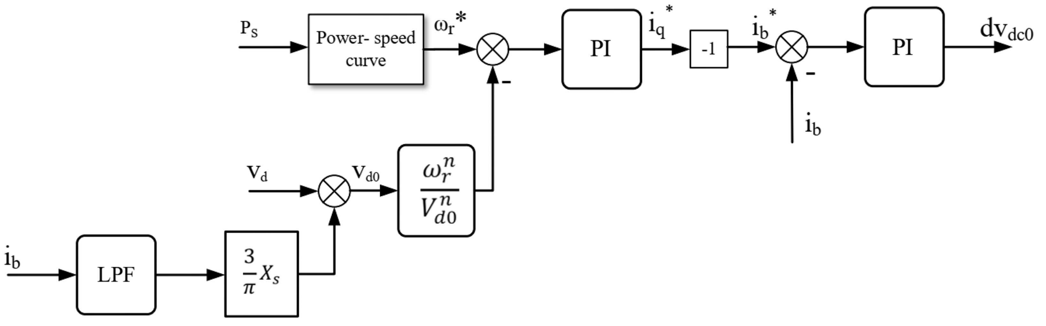

Figure 10. Overall block diagram of the boost converter control.

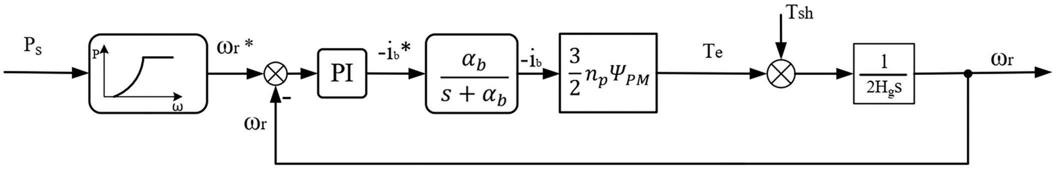

Figure 11. Outer speed control loop at the first control strategy.

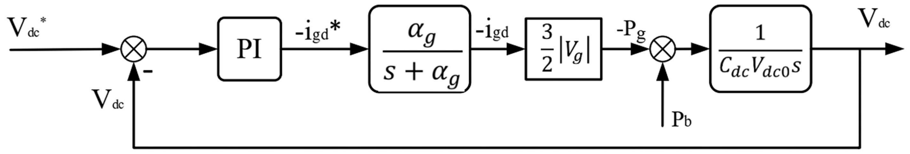

Figure 12. Closed loop control of the dc-link voltage with the first control strategy.

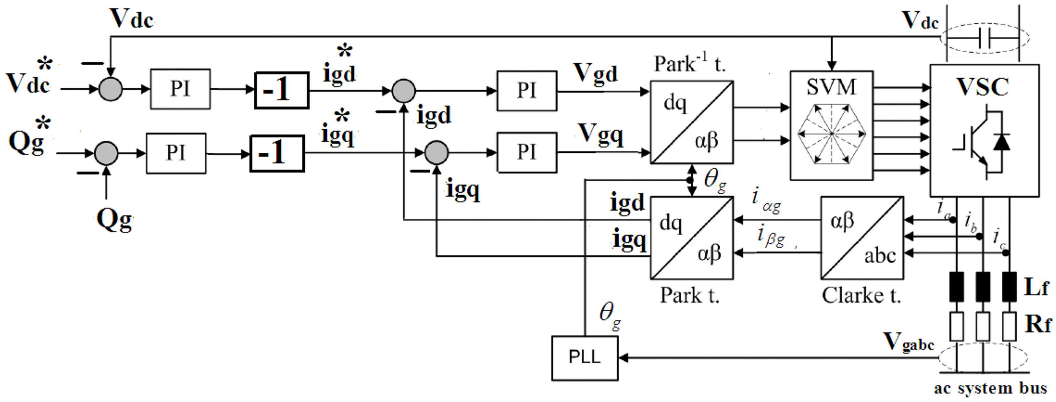

Figure 13. Overall control structure of the GSC in the first control strategy.

rotational speeds below the rated one. At high wind speeds, the MPPT mode is not realized and generator speed is set to its rated one. The stator output active power at the MPPT mode may be considered as $P_s = k_{opt}{\omega_r}^3$.

4.2.2. GSC control with the first control strategy

In the first control strategy, the GSC can set the dc-link voltage at the reference value. As stated before, the GSC is controlled in the *dq* frame with GVO, and thus in Figure 1, the active power injected to the grid can be given as $P_g = v_{gd}i_{gd}$. From Figure 1 and by ignoring the converters losses, the dc-link power balance equation is expressed as:

$$(P_b - P_g) = C_{dc}v_{dc}\frac{dv_{dc}}{dt}, \tag{18}$$

where P_b is the boost converter input active power, v_{dc} and C_{dc} are the dc-link voltage (in volt) and capacitor (in F). Linearizing Eq. (18) around the operating point results in the following equation:

$$(\Delta P_b - \Delta P_g) = C_{dc}v_{dc0}\frac{d\Delta v_{dc}}{dt}, \tag{19}$$

where Δ depicts the small-signal deviation about the operating point. Figure 12 illustrates the closed-loop control of the dc-link voltage. The term $\alpha_g/(s+\alpha_g)$ in Figure 12 corresponds to the closed-loop transfer function of the inner current control loop. If the dc-link dynamics is slow enough compared to the inner current control loop, we can set i_{gd} to its set point value i_{gd}^*, and thus for the frequency range of $\omega << \alpha_g$, the dynamics of $\alpha_g/(s+\alpha_g)$ in Figure 12 can be ignored. Therefore, the transfer function from v_{dc}^* to v_{dc} may be described by:

$$\frac{v_{dc}}{{v_{dc}}^*} = \frac{2\xi\omega_n s + {\omega^2}_n}{s^2 + 2\xi\omega_n s + {\omega^2}_n}, \tag{20}$$

where ω_n and ξ correspond to the closed-loop bandwidth and the damping ratio of the dc-link voltage control loop, respectively and ${\omega^2}_n = 3\,|V_g|\,k_{i\_dc}/2C_{dc}V_{dc0}$, $2\xi\omega_n = 3\,|V_g|\,k_{p\_dc}/2C_{dc}V_{dc0}$.

In the grid voltage oriented reference frame, i_{gd} can be used for the dc-link voltage control and i_{gq} for the reactive power control. Usually i_{gq}^* is considered equal to zero and thus the GSC works at unity power factor. Figure 13 demonstrates the overall control structure of the GSC in the first control strategy.

4.3. System control structure at the second control strategy

In the second control strategy, the boost converter is responsible for the control of the PMSG output active power. Considering Eq. (8) and Figure 5 and under disregarding the stator resistance, the PMSG active power may be given by:

$$P_s = -\frac{3}{2}\omega_r\psi_{pm}i_{sq}. \tag{21}$$

As shown in Section 3, $i_{sq} = -i_b$, and thus the PMSG active power in terms of the boost converter current may be given as:

$$P_s \cong \frac{3}{2}\omega_r\psi_{pm}i_b. \tag{22}$$

The linearized form of Eq. (22) about the operating point can be given as:

$$\Delta P_s = \left(\frac{3}{2}\omega_{r0}\psi_{pm}\right)\Delta i_b + \left(\frac{3}{2}\psi_{pm}i_{b0}\right)\Delta\omega_r. \tag{23}$$

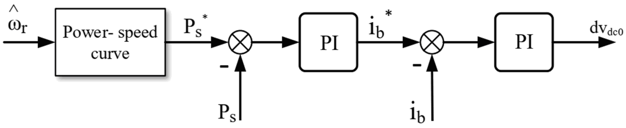

Figure 14. Overall control block diagram of the boost converter in the second control strategy.

Figure 14 demonstrates the overall control block diagram of the boost converter in the second control strategy. The boost converter control structure includes the outer and inner control loops of the PMSG active power and boost converter current, respectively.

From Eq. (23), the PMSG active power control loop is achieved as given in Figure 15. In Figure 15, $\alpha_b/(s+\alpha_b)$ is the current control loop transfer function of the boost converter.

From Figure 15, the closed-loop transfer function of the PMSG active power control is attained as given below:

$$\frac{P_s}{P_s{}^*}=\frac{\left(\frac{3}{2}k_{pP}\omega_{r0}\psi_{pm}\alpha_b\right)s+\left(\frac{3}{2}k_{iP}\omega_{r0}\psi_{pm}\alpha_b\right)}{s^2+\alpha_b\left(1+\frac{3}{2}k_{pP}\omega_{r0}\psi_{pm}\right)s+\left(\frac{3}{2}k_{iP}\omega_{r0}\psi_{pm}\alpha_b\right)}. \tag{24}$$

According to Eq. (24), the PI controller parameters k_{pP} and k_{iP} are obtained from the following equation:

$$2\xi\omega_n=\alpha_b\left(1+\frac{3}{2}k_{pP}\omega_{r0}\psi_{pm}\right),$$

$$\omega_n{}^2=\left(\frac{3}{2}k_{iP}\omega_{r0}\psi_{pm}\alpha_b\right), \tag{25}$$

where ω_n and ξ correspond to the undamped natural frequency and damping ratio of the PMSG active power control loop, respectively. Since the outer control loop should be much slower than the inner control loop, by selecting $\omega_n=0.1\alpha_b$ and $\xi=0.7$, the controller parameters are achieved. In Figure 15, the reference power P_s^* is selected such that the WT operates in the MPPT mode at the rotational speeds below the rated one. At high wind speeds, the WT cannot operate in the MPPT mode and PMSG active power is set to its rated value. As stated before, the stator output active power at the MPPT mode can be approximated as $P_s=k_{opt}\omega_r{}^3$.

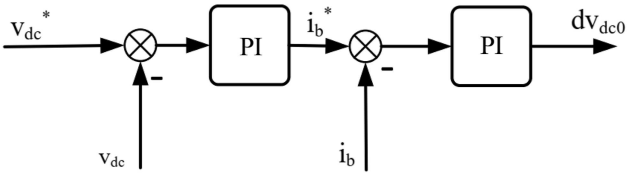

Figure 16. Overall control of the boost converter in the third control strategy.

The main function of the GSC in the second control strategy is keeping the dc-link voltage constant and regulation of the reactive power delivered to the grid. Hence, the control structures of the GSC in the first and second control strategies are exactly similar, and thus, are not given in this section.

4.4. System control structure at the third control strategy

In the following, the control block diagrams of the boost converter and GSC at the third control strategy are presented.

4.4.1. Boost converter control at the third control strategy

In the third control strategy, the boost converter regulates the dc-link voltage to the set point value. According to Figure 2, the dc-link voltage dynamics can be described by:

$$(1-d)\,i_b-i_{dc}=C_{dc}\frac{dv_{dc}}{dt}. \tag{26}$$

The linearized form of Eq. (26) about the operating point can be given as:

$$(1-d_0)\,\Delta i_b-\Delta d.i_{b0}-\Delta i_{dc}=C_{dc}\frac{d\Delta v_{dc}}{dt}. \tag{27}$$

Figure 16 demonstrates the overall boost converter control in the third control strategy. The boost converter control structure includes the outer and inner control loops of the dc-link voltage and boost converter current, respectively.

From Eq. (27), the dc-link voltage control loop by the boost converter is attained as given in Figure 17. In Figure 17, $\alpha_b/(s+\alpha_b)$ represents the transfer function related to boost converter current control loop.

If dynamics of the dc-link is slow enough compared to the inner current control loop, we can set i_b equal to set point value i_b^*, and therefore for the

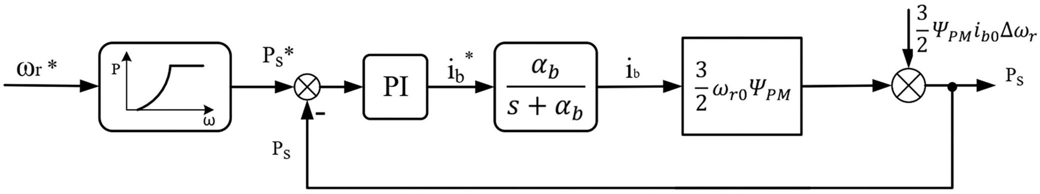

Figure 15. Outer PMSG active power control loop with the second control strategy.

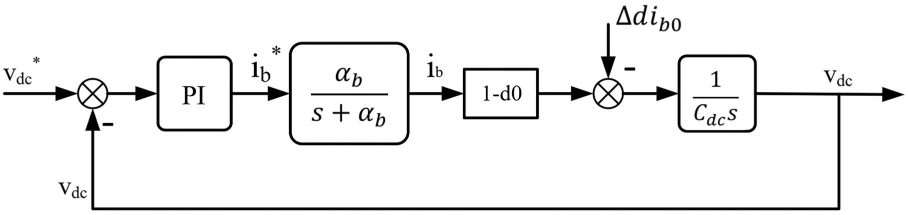

Figure 17. Outer control loop related to dc-link voltage with the third control strategy.

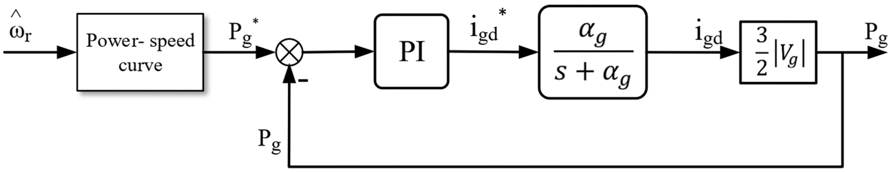

Figure 18. Control loop of the GSC active power.

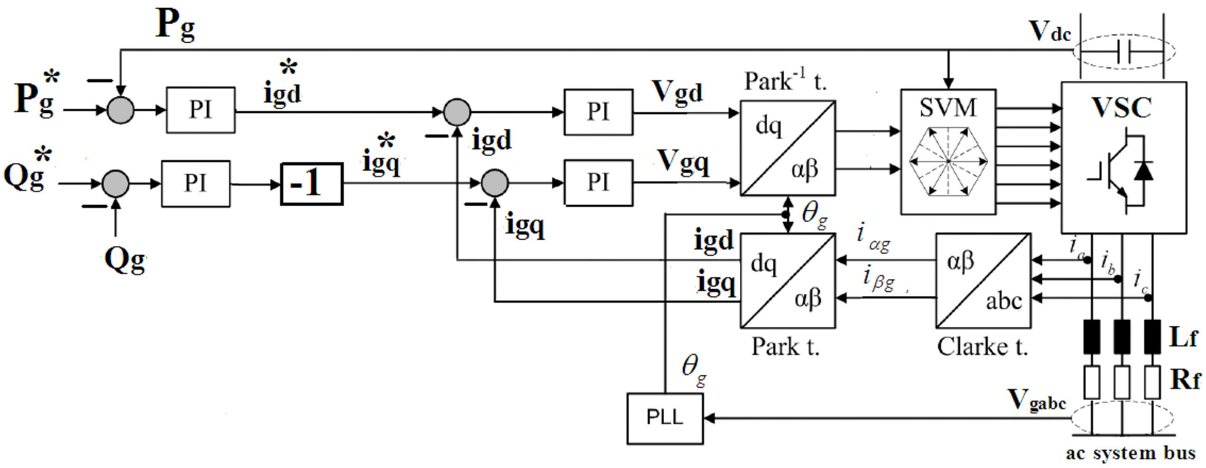

Figure 19. Overall control structure of the GSC in the third control strategy.

frequency range $\omega << \alpha_b$, the dynamics of $\alpha_b/(s+\alpha_b)$ in Figure 17 can be ignored. Therefore, the transfer function from v_{dc}^* to v_{dc} may be given as:

$$\frac{v_{dc}}{v_{dc}^*} = \frac{2\xi\omega_n s + \omega^2{}_n}{s^2 + 2\xi\omega_n s + \omega^2{}_n}, \tag{28}$$

where ω_n and ξ correspond to the bandwidth and damping ratio of the dc-link voltage control loop, respectively and:

$$\omega^2{}_n = k_i(1-d_0)/C_{dc},$$

$$2\xi\omega_n = k_p(1-d_0)/C_{dc}.$$

4.4.2. GSC control structure with the third control strategy

In the third control mode, the GSC sets the grid injected active and reactive powers to their reference values. As stated before, in the grid voltage oriented reference frame, i_{gd} and i_{gq} are used for the active and reactive power regulation, respectively. Figure 18 demonstrates the control loop of the GSC active power.

P_g^* in Figure 18 is the GSC active power reference and is selected for operation of the WT in the MPPT mode. For operation in the MPPT mode and under neglecting the converter losses, P_g^* may be considered as $k_{opt}{\omega_r}^3$ for the generator speed blow the rated one. Figure 19 illustrates the overall block diagram of the GSC control system in the third control mode, where i_{gd} controls P_g and i_{gq} is adjusted to zero for operation at unity power factor.

5. Simulation results

Performance of the PMSG-WT in the study system of Figure 1 is examined in this section, and capabilities of the three control strategies presented in Section 4 are investigated and compared. The study system in Figure 1 includes a 2 MW-690 V-50 Hz PMSG-based WT with parameters of Appendix A that is linked to a 20 kV grid through a 690 V/20 kV transformer and transmission line.

Figure 20 demonstrates the wind speed profile and corresponding generator speed response. Figure 20(b)

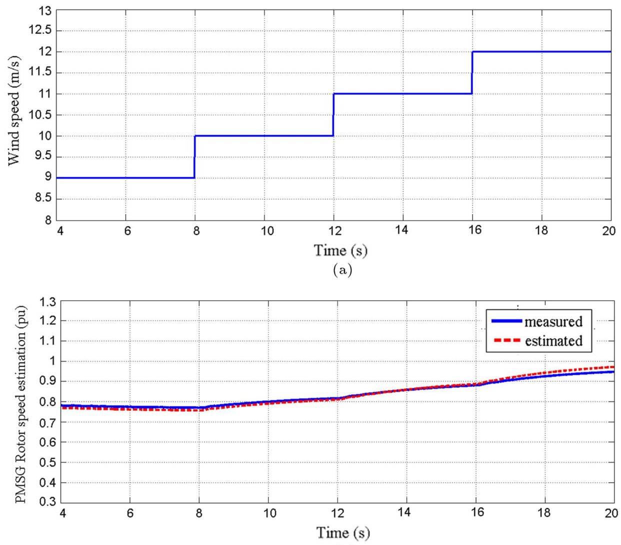

(a)

(b)

Figure 20. (a) wind speed profile and (b) actual and estimated responses of the generator speed against wind speed profile of Figure 20(a).

indeed depicts the estimated and actual values of the generator speed, and based on which, it is clear that the estimated values of the generator speed at different wind speed are well close to the actual ones.

Figure 21 shows steady state responses of the PMSG-based WT for the three mentioned control strategies mentioned in Section 4 and against wind speed change from 10 to 12 m/s. Figure 21 indeed illustrates responses of the generator speed, stator active power, dc-link voltage and electromagnetic torque. From Figure 21, it is evident that WT responses are relatively identical for all three control strategies mentioned in Section 4.

Figure 22 shows the three-phase and dq parts of the stator current and boost converter current for the wind speed of 12 m/sec. In Figure 22, because of existence of the diode-rectifier, the three-phase stator currents contain the fundamental and harmonic frequencies. Therefore, as shown in Figure 22(a) and (b), i_{sd} and i_{sq} are not constant and include ac harmonic ripples. In Figure 22, the mean values of i_{sq} and boost converter current i_b are approximately identical and equal to 2590 A, and this is in close agreement with the result of Section 3.

Figure 23 describes responses of the dc-link voltage, stator active power, generator torque and boost converter current against 70% three-phase voltage dip at $t = 4$ sec, for the three mentioned control strategies. Also, Figure 24 shows the WT time responses under 90% three-phase voltage dip, for all three mentioned control strategies.

As stated before, in the first control strategy, the boost converter is responsible for the generator speed control and GSC adjusts the dc-link voltage at its reference value. In the second control strategy, the boost converter sets the PMSG active power at the reference value, and GSC adjusts the dc-link voltage to its set point value. In the third control strategy, the boost converter adjusts the dc-link voltage at the reference value, and GSC controls the injected active power to the grid to a reference value corresponding to the MPPT mode.

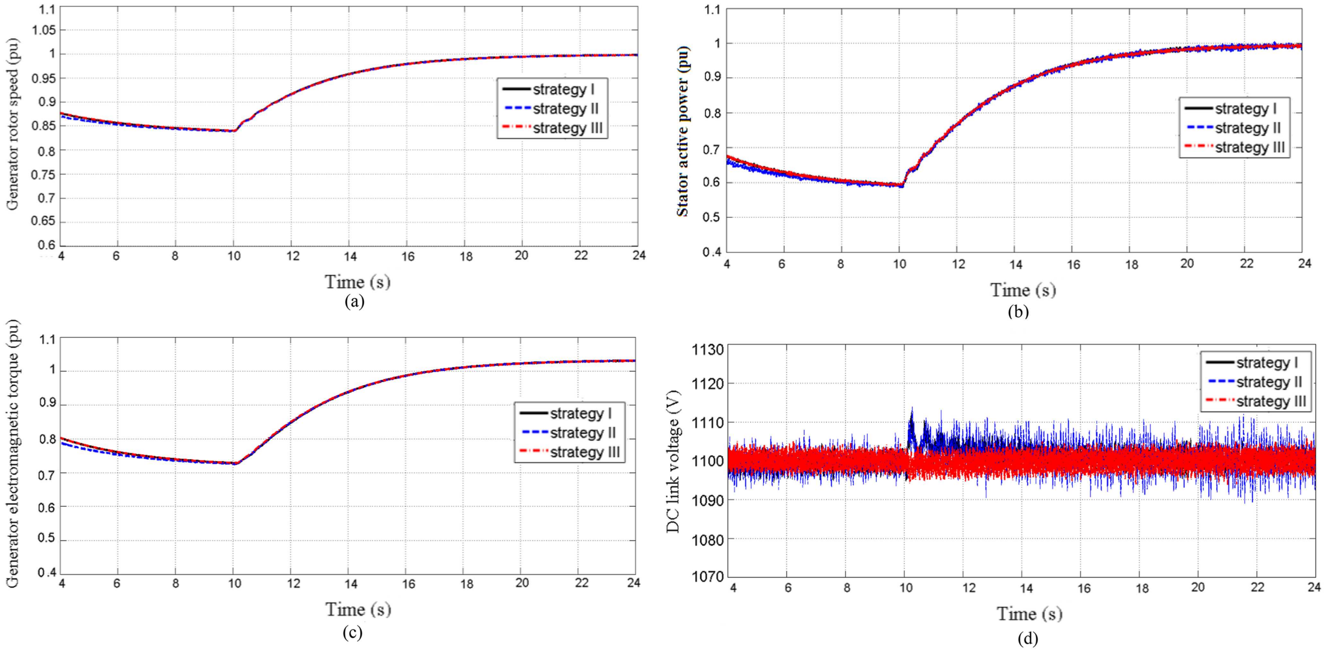

(a)

(b)

(c)

(d)

Figure 21. System time responses with the mentioned three control strategies and against the wind speed change from 10 to 12 m/s, (a) generator speed, (b) stator active power, (c) electromagnetic torque, and (d) dc-link voltage.

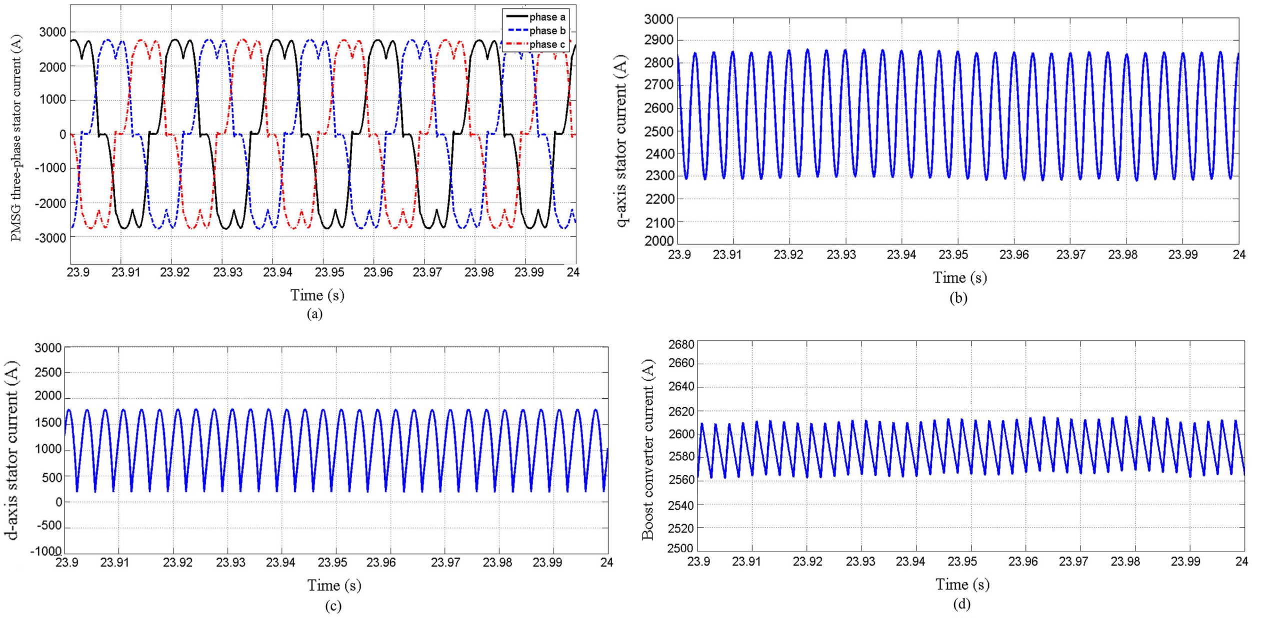

Figure 22. Time responses of the PMSG-based WT at wind speed of 12 m/s, (a) three-phase stator current, (b) d-axis stator current, (c) q-axis stator current, and (d) boost converter current.

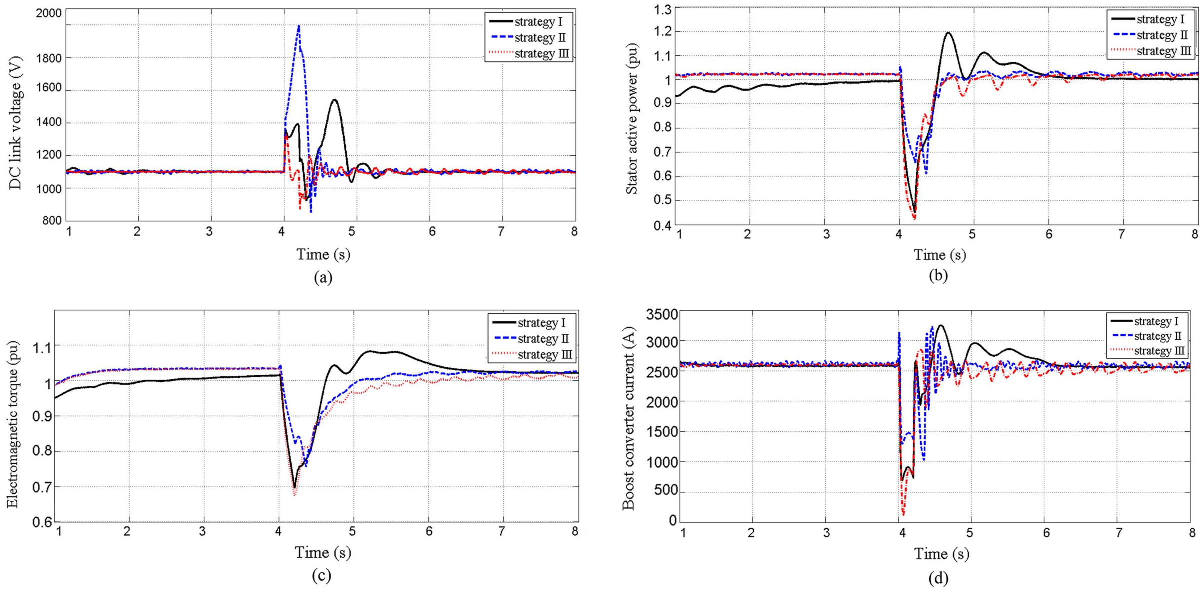

Figure 23. System time responses with the mentioned three control strategies against 70% grid voltage dip at $t = 4$ s, (a) dc-link voltage, (b) stator active power, (c) electromagnetic torque, and (d) boost converter current.

According to Figure 23(a) and under 70% voltage dip, the peak values of the dc-link voltage during the fault for the first, second and third control strategies are 1550 v, 2000 v and 1350 v, respectively. Also, according to Figure 24(a) and under 90% voltage dip, the peak values of the dc-link voltage for the first, second and third control strategies are 2000 v, 2420 v and 1400 v, respectively.

According to Figures 23(a) and 24(a), it is clear that the peak values of the dc-link voltage during the fault for the third control strategy are lower than the ones in the first and second control strategies. Hence, the LVRT capability of the wind-turbine enhances significantly in the third control structure without any hardware protection. Since, in the third control structure, MSC is responsible for the dc-link voltage control via q-axis stator current, the stator output active power, generator torque and boost converter current decrease during the voltage dip in this control structure (see, Figure 23(b)–(d) and Figure 24(b)–(d)).

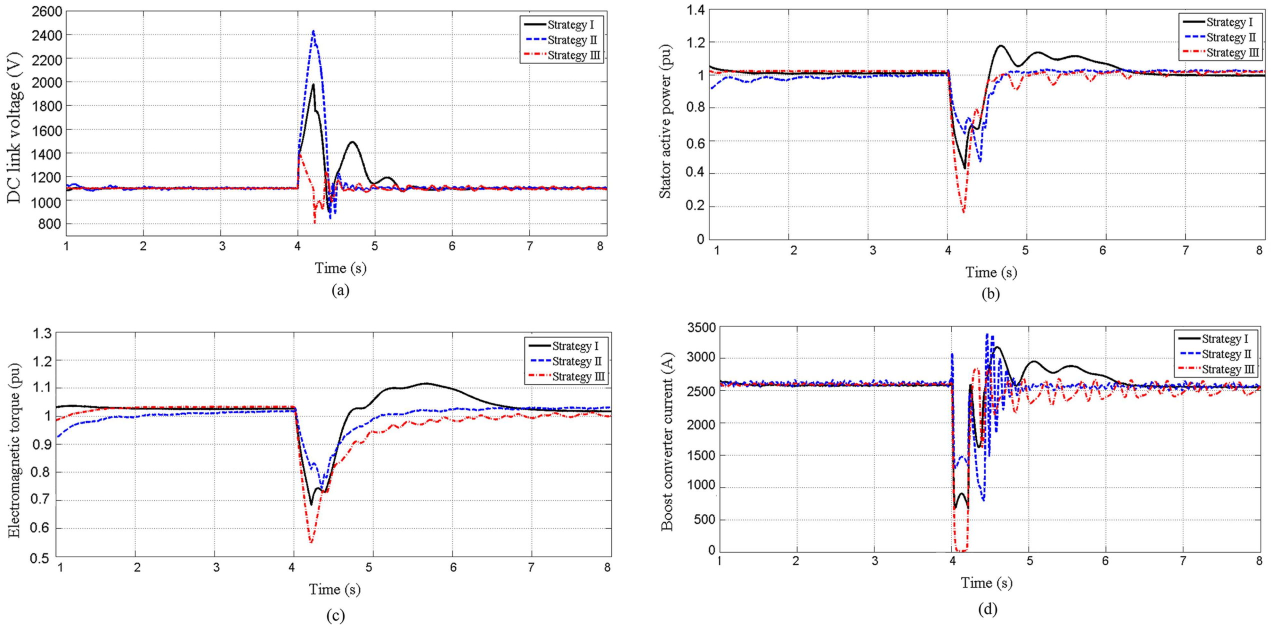

Figure 24. System time responses with the mentioned three control strategies against 90% grid voltage dip at $t = 4$ s (a) dc-link voltage, (b) stator active power, (c) electromagnetic torque, and (d) boost converter current.

Hence, according to Figures 23(b) and 24(b), in the third control structure, the power exported from the stator to the dc-link decreases during the voltage dip, and this lessens the dc-link overvoltage in the third control structure during fault conditions.

6. Conclusion

In this paper, performance analysis and control of the PMSG-WT, implementing boost converter and diode-rectifier as the machine-side converter, is presented. In the paper, at first, the relation between the active component of the stator current and boost converter current is extracted, a simple and efficient approach is presented for the generator speed estimation, and then, three sensorless control strategies are presented for the control of the grid-connected PMSG-based Wind Turbine (WT).

At the end, features of the abovementioned three control strategies are investigated and compared against wind speed variation and grid voltage dip. In this way, steady-state and transient responses of the WT system are investigated for each mentioned control strategy in the MATLAB-Simulink environment. It is shown that steady-state responses of the WT are relatively identical for all three control strategies. However, at the fault conditions, the third control strategy has better performance, and thus, the WT low-voltage ride-through behavior enhances significantly in the third control structure without any hardware protection. This is because in the third control structure, the boost converter is responsible for the dc-link voltage control, and thus, the stator output active power, generator torque and boost converter current decrease during the voltage dip in this control structure Therefore, the power exported from the Permanent Magnet Synchronous Generator (PMSG) stator to the dc-link decreases during the voltage dip, and this lessens the dc-link overvoltage, in the third control structure, during the grid fault conditions.

Nomenclature

PMSG	Permanent Magnet Synchronous Generator
WT	Wind Turbine
MSC	Machine Side Converter
GSC	Grid Side Converter
LVRT	Low Voltage Ride-Through
$v_{dq}, i_{dq}, \psi_{dq}$	dq-components of the stator voltage, current and flux
ψ_{pm}	Stator flux linkage
E_g	Back-emf voltage of the stator
p, n_p	Number of generator poles and number of pole pairs
R_s, L_s, X_s	Stator resistance, synchronous inductance and synchronous reactance
T_e, ω_r	Generator torque and rotational speed
v_d, v_{dc}	Input and output voltage of boost converter
C_{dc}	dc-link capacitor
R_b, L_b	Boost converter resistance and inductance

Table A.1. System under study parameters.

Component	Parameter	Value
PMSG WT parameters	Rated power	2 MW
	Rated stator voltage	690 V
	Rated frequency	50 Hz
	Number of pole pairs	4
	ψ_{pm}	0.95 pu
	R_s	0.002 pu
	$L_s = L_d = L_q$	0.14 pu
	H_g,H_t,	0.6 sec, 4 sec
WT tansformer parameters 690 V/20 kV	X_{trans}	0.1 pu
Boost converter parameters	R_b, L_b	5 Ω, 2.4 mH
GSC parameters	dc-link voltage Vdc	1100 V
	dc-link capacitor Cdc	90 mF
	GSC output LC filter L_F, C_F	0.15 pu, 0.07 pu

d	Duty cycle of the boost converter switch
i_b	Boost current
v_{GSCdq},	dq-components of the GSC output
i_{gdq}, v_{gdq}	voltage and current and grid voltage
R_f, L_f	Filter resistance and inductance
P_s, P_g	PMSG output active power and GSC output active power
H_g	Generator inertia constant

Appendix A

Parameters of the 2 MW, 690 V, 50 Hz, PMSG-WT are given in Table A.1.

References

1. Uehara, A., Pratap, A., Goya, T., et al. "A coordinated control method to smooth wind power fluctuations of a PMSG-based WECS", *IEEE Transactions on Energy Conversion*, **26**(2), pp. 550–558 (2011).
DOI: 10.1109/TEC.2010.2091819
2. Kasem Alaboudy, A.H., Daoud, A.A., Desouky, S.S., et al. "Converter controls and flicker study of PMSG-based grid connected wind turbines", *Ain Shams Engineering Journal*, **4**(1), pp. 75–91 (2013).
DOI: 10.1016/j.asej.2012.05.004
3. Rajaei, A.H., Mohamadian, M., Dehghan, S.M., et al. "PMSG-based variable speed wind energy conversion system using Vienna rectifier", *European Transactions on Electrical Power*, **21**(1), pp. 954–972 (2011).
DOI: 10.1002/etep.414
4. Freire, N.M.A. and Cardoso, A.J.M. "Fault-tolerant PMSG drive with reduced DC-link ratings for wind turbine applications", *IEEE Journal of Emerging and Selected Topics in Power Electronics*, **2**(1), pp. 26–34 (2014).
DOI: 10.1109/JESTPE.2013.2293632
5. Zhang, S., Tseng, K.J., Vilathgamuwa, D.M., et al. "Design of a robust grid interface system for PMSG-based wind turbine generators", *IEEE Transactions on Industrial Electronics*, **58**(1), pp. 316–328 (2011).
DOI: 10.1109/TIE.2010.2044725
6. Rahimi, M. "Mathematical modeling, dynamic response analysis and control of PMSG based wind turbines operating with an alternative control structure in power control mode", *International Transactions on Electrical Energy Systems*, **27**(12), pp. 1–18 (2017).
DOI: 10.1002/etep.2346
7. Rahimi, M. and Beiki, A. "Efficient modification of the control system in PMSG based wind turbine for improvement of the wind turbine dynamic response and suppression of torsional oscillations", *International Transactions on Electrical Energy Systems*, **28**(8), pp. 1–16 (2018).
DOI: 10.1002/etep.2591
8. Rahimi, M. "Modeling, control and stability analysis of grid connected PMSG based wind turbine assisted with diode rectifier and boost converter", *International Journal of Electrical Power & Energy Systems*, **93**, pp. 84–96 (2017).
DOI: 10.1016/j.ijepes.2017.05.024
9. Xie, D., Lu, Y., Sun, J., et al. "Small signal stability analysis for different types of PMSGs connected to the

grid", *Renewable Energy*, **106**, pp. 149–164 (2017). DOI: 10.1016/j.renene.2017.01.026

10. Noori Khezrabad, A. and Rahimi, M. "Performance and dynamic response enhancement of PMSG- based wind turbines employing boost converter-diode rectifier as the machine-side converter", *Scientia Iranica*, **29**(3), pp. 1523–1536 (Jun. 2022). DOI: 10.24200/sci.2020.54375.3722.
11. Urtasun, A., Sanchis, P., San Martín, I., et al. "Modeling of small wind turbines based on PMSG with diode bridge for sensorless maximum power tracking", *Renewable Energy*, **55**, pp. 138–149 (2013). DOI: 10.1016/j.renene.2012.11.038
12. Aubrée, R., Auger, F., Macé, M., et al. "Design of an efficient small wind-energy conversion system with an adaptive sensorless MPPT strategy", *Renewable Energy*, **86**, pp. 280–291 (2016). DOI: 10.1016/j.renene.2015.08.030
13. Şerban, I. and Marinescu, C. "A sensorless control method for variable-speed small wind turbines", *Renewable Energy*, **43**, pp. 256–266 (2012). DOI: 10.1016/j.renene.2011.11.032
14. Yu, K.N. and Liao, C.K. "Applying novel fractional order incremental conductance algorithm to design and study the maximum power tracking of small wind power systems", *Journal of Applied Research and Technology*, **13**(2), pp. 238–244 (Apr. 2015). DOI: 10.1016/j.jart.2015.06.002
15. Mozayan, S.M., Saad, M., Vahedi, H., et al. "Sliding mode control of PMSG wind turbine based on enhanced exponential reaching law", *IEEE Transactions on Industrial Electronics*, **63**(10), pp. 6148–6159 (2016). DOI: 10.1109/TIE.2016.2573265
16. Dursun, E.H. and Kulaksiz, A.A. "Second-order sliding mode voltage-regulator for improving MPPT efficiency of PMSG-based WECS", *International Journal of Electrical Power & Energy Systems*, **121**, p. 106149 (2020). DOI: 10.1016/j.ijepes.2020.106149
17. Liang, C., Le Claire, J.-C., Aït-Ahmed, M., et al. "Power control of 5-phase PMSG-diode rectifier-interleaved boost set under health and fault modes", *Electric Power Systems Research*, **152**, pp. 316–322 (2017). DOI: 10.1016/j.epsr.2017.07.003
18. Yaramasu, V., Wu, B., Alepuz, S., et al. "Predictive control for low-voltage ride-through enhancement of three-level-boost and NPC-converter-based PMSG wind turbine", *IEEE Transactions on Industrial Electronics*, **61**(12), pp. 6832–6843 (2014). DOI: 10.1109/TIE.2014.2327580
19. Yaramasu, V. and Wu, B. "Predictive control of a three-level boost converter and NPC inverter for high-power PMSG-based medium voltage wind energy conversion systems", *IEEE Transactions on Power Electronics*, **29**(10), pp. 5308–5322 (2014). DOI: 10.1109/TPEL.2013.2295292
20. Milev, K., Yaramasu, V., Dekka, A., et al. "Predictive control of multichannel boost converter and VSI-based six-phase PMSG wind energy systems with fixed switching frequency", *11th Power Electronics, Drive Systems, and Technologies Conference (PEDSTC)*, pp. 1–6 (2020). DOI: 10.1109/PEDSTC49159.2020.9088417
21. Milev, K., Alshammari, F., Yaramasu, V., et al. "Predictive control with fixed switching frequency for three-level boost and NPC converters interfaced PMSG wind turbine", *3rd International Conference on Energy, Power and Environment: Towards Clean Energy Technologies*, pp. 1–6 (2021). DOI: 10.1109/ICEPE50861.2021.9404400
22. Barote, L., Marinescu, C., and Cirstea, M.N. "Control structure for single-phase stand-alone wind-based energy sources", *IEEE Transactions on Industrial Electronics*, **60**(2), pp. 764–772 (2013). DOI: 10.1109/TIE.2012.2203762
23. Mesbahi, A., Saad, A., Khafallah, M., et al. "Boost converter analysis to optimize variable speed PMSG wind generation system", *International Renewable and Sustainable Energy Conference (IRSEC)*, pp. 275–280 (2013). DOI: 10.1109/IRSEC.2013.6529647
24. Putri, R.I., Pujiantara, M., Priyadi, A., et al. "Maximum power extraction improvement using sensorless controller based on adaptive perturb and observe algorithm for PMSG wind turbine application", *IET Electric Power Applications*, **12**(4), pp. 455–462 (2018). DOI: 10.1049/iet-epa.2017.0531
25. Alsokhiry, F., Abdelsalam, I., Adam, G.P., et al. "High-power medium-voltage three-phase ac-dc buck-boost converter for wind energy conversion systems", *Electric Power Systems Research*, **177**, p. 106012 (2019). DOI: 10.1016/j.epsr.2019.106012
26. Chinchilla, M., Arnaltes, S., and Burgos, J.C. "Control of permanent-magnet generators applied to variable-speed wind-energy systems connected to the grid", *IEEE Transactions on Energy Conversion*, **21**(1), pp. 130–135 (2006). DOI: 10.1109/TEC.2005.852893
27. Tripathi, S.M., Tiwari, A.N., and Singh, D. "Optimum design of proportional-integral controllers in grid-integrated PMSG-based wind energy conversion system", *International Transactions on Electrical Energy Systems*, **26**(5), pp. 1006–1031 (2016). DOI: 10.1002/etep.2176
28. Zhang, X., Wu, Z., Hu, M., et al. "Coordinated control strategies of VSC-HVDC-based wind power systems for low voltage ride through", *Energies*, **8**(7), pp. 7224–7242 (2015). DOI: 10.3390/en8077224
29. Dang, C.-L., Zhang, L., and Zhou, M.-X. "Optimal power control model of direct driven PMSG", *Energy Procedia*, **12**, pp. 844–848 (2011). DOI: 10.1016/j.egypro.2011.10.112

30. Alizadeh, O. and Yazdani, A. "A control strategy for power regulation in a direct-drive WECS with flexible drive-train", *IEEE Transactions on Sustainable Energy*, **5**(4), pp. 1156–1165 (2014). DOI: 10.1109/TSTE.2014.2342188

31. Hansen, A.D. and Michalke, G. "Modelling and control of variable-speed multi-pole permanent magnet synchronous generator wind turbine", *Wind Energy*, **11**(5), pp. 537–554 (2008). DOI: 10.1002/we.278

32. Yuan, X., Wang, F., Boroyevich, D., et al. "DC-link voltage control of power converter for wind generator operating in weak-grid systems", *IEEE Transactions on Power Electronics*, **24**(9), pp. 2178–2192 (2009). DOI: 10.1109/TPEL.2009.2022522

33. Hansen, A.D. and Michalke, G. "Multi-pole permanent magnet synchronous generator wind turbines' grid support capability in uninterrupted operation during grid faults", *IET Renewable Power Generation*, **3**(3), pp. 333–348 (2009). DOI: 10.1049/iet-rpg.2008.0054

34. Van, T.L., Ngyen, T.D., Tran, T.T., et al. "Advanced control strategy of back-to-back PWM converters in PMSG wind power system", *Advances in Electrical and Electronic Engineering,* **13**(2), pp. 81–95 (2015). DOI: 10.15598/aeee.v13i2.1287

35. Nguyen, P.T.H., Stüdli, S., Braslavsky, J.H., et al. "Coordinated control for low voltage ride through in PMSG wind turbines", *IFAC-PapersOnLine*, **51**(28), pp. 672–677 (2018). DOI: 10.1016/j.ifacol.2018.11.374

36. Mohan, N., Undeland, T.M., and Robbins, W.P., *Power Electronics: Converters, Applications, and Design*, 3rd edition, Wiley (2002).

Biographies

Yahya Abdollahi received his BSc degree in Electrical Engineering in 2004 from Isfahan University of Technology, Isfahan, Iran. He obtained the MSc degree in Electrical Engineering from Shahrekord University, Shahrekord, Iran in 2011. He is currently working towards the PhD degree at University of Kashan, Kashan, Iran. His research interests include power electronics, dynamic modeling and stability analysis of grid-interactive power converters, wind turbines and microgrids.

Mohsen Rahimi received his BSc degree in Electrical Engineering in 2001 from Isfahan University of Technology, Isfahan, Iran. He obtained both his MSc and PhD degrees in Electrical Engineering from Sharif University of Technology (SUT), Tehran, Iran, in 2003 and 2011, respectively. He joined the Department of Electrical and Computer Engineering at University of Kashan, Kashan, Iran, as an Assistant Professor, in 2011. Currently, he is an Associate Professor at University of Kashan, and his major research interests include modeling and control of renewable energy sources, wind turbines and microgrids.

Abolfazl Halvaei Niasar received his BSc, MSc, and PhD in 1996, 1999, and 2008 from Isfahan University of Technology (IUT), University of Tehran (UT) and Iran University of Science and Technology (IUST) all in Electrical Engineering respectively. He is currently with the Department of Electrical and Computer Engineering, at University of Kashan, Kashan, Iran. His research interests are mainly PM and Brushless DC motor drives, sensorless drives, design and analysis of Electrical machines, DSP based control systems and industrial control systems engineering.